K-region tetrasubstituted deep-blue pyrene-based luminogens: Visual detection of trace nitro-explosives

Jing-Yi Cao,[a] Ze-Dong Yu,[a] Guang Yang,[a] Xue-Can wang,[a] Lu Jiang,[a] Xi Wang,[a] Wen-Xuan Zhao,[a] Shu-Hai Chen,[a] Carl Redshaw,[c] and Chuan-Zeng Wang[a,*] Takehiko Yamato,[b,*]

[a.] School of Chemistry and Chemical Engineering, Shandong University of Technology, Zibo 255049, P. R. China

[b.] Department of Applied Chemistry, Faculty of Science and Engineering, Saga University Honjo-machi 1, Saga 840-8502 Japan

[c.] Chemistry, School of Natural Sciences, The University of Hull, Cottingham Road, Hull, Yorkshire HU6 7RX, UK

Abstract:

In recent years, fluorescence sensors have been widely used in explosive detection due to their portability and high efficiency. In the present work, two K-region tetrasubstituted deep-blue pyrene-based luminogens were designed and synthesized by introducing electron-donating groups. The optical properties were investigated by experimental and density functional theory (DFT) methods. Reasonable luminescence efficiency and electron rich characteristic allowed for the possible detection of nitro-explosives. Both luminogens, especially **TFPy**, exhibit a sensitive response towards nitroanilines (**NA**), with a limit of detection (LOD) for ***p*-NA** as low as 2.75×10^{-8} M, which is mainly attributed to the electron-donating substituents on the periphery of the pyrene core and the extended π-conjugated structure. These research results establish a low-cost and simple strategy for the detection of trace nitro-explosives.

Keywords: K-region; Pyrene chemistry; Sensing properties; Nitro-explosives; Visualization

1. Introduction

The rapid development of society and the ever-growing material and spirit cultural needs inspires a desire for security, including in transportation, the environment and in day-to-day life. However, various security factors have become challenging problems that need to be solved urgently. For instance, the threat posed by potentially ubiquitous nitro-explosives is one of the most important factors [1–3]. Thus, explosive detection with ultra-selectivity, super-sensitivity and a fast response time has aroused great research interest. In this context, Raman spectroscopy, gas chromatography-electron capture detection, thermal neutron analysis and ion mobility spectroscopy have been employed as viable methods for the detection and/or quantification of nitro-explosives [4–7]. However, some deficiencies in these methods, such as lack of sensitivity and portability [8], have led to the development of more efficient detection methods. As one of the most competitive candidates, optical chemosensors are used for the trace detection of nitro explosives in recent years [9–12]. Such research focuses on the design and synthesis of high-efficiency fluorescent probes with excellent sensitivity, portability and real-time monitoring [13]. Generally speaking, fluorescence quenching as the main sensory phenomenon was widely used, which is primarily driven by Förster resonance energy transfer (FRET), intramolecular charge transfer (ICT), the inner filter effect (IFE) and photoinduced electron transfer (PET) mechanism [14–18]. So, the design and synthesis of high efficiency luminogents remains a challenging yet desirable topic in materials science.

Polycyclic aromatic hydrocarbons (PAHs) have similar structural characteristics with multiple aromatic rings, significant electron-donating properties and high fluorescence quantum efficiency [19,20]. This results in the formation of non-fluorescent charge-transfer complexes with electron-deficient molecules. Thus, PAHs are an important class of fluorescent small molecule sensing materials in nitro-explosives detection, especially for nitroaromatics (NACs) detection applications [21–23]. Pyrene and its derivatives, as typical PAHs, have also been widely used in the detection of nitro-explosives because of their remarkable electron-donating properties and high fluorescence quantum efficiency [24–26]. Given this, the purposeful design of

appropriate luminogents is also a main strategy of current research in fluorescence based explosive detection, and is conducive to the formation of non-fluorescent charge-transfer complexes with nitro-explosives [27,28].

In the present work, two K-region tetrasubstituted deep-blue pyrene-based luminogens were synthesized by introducing multiple electron-donating substituents (Scheme 1). It is worth mentioning that both two luminogents displayed excellent detection for nitroaniline (**NA**) isomers, which is different from other reported work for the selective detection of different types of nitro-explosives [29–31]. An efficient strategy for the visual selective detection of trace *meta*-nitroaniline (***m*-NA**) with a low limit of detection is presented.

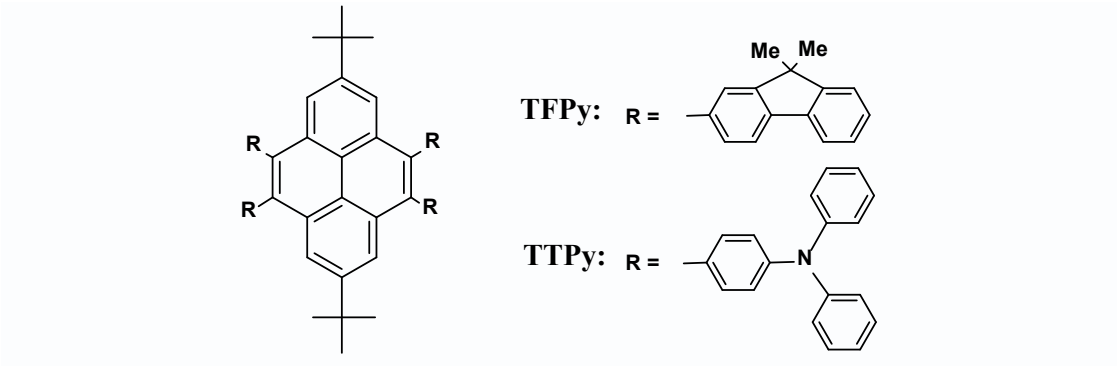

Scheme 1. Chemical structures of **TFPy** and **TTPy**.

2. Experimental Section

2.1. Materials and methods

All chemicals were purchased from commercial suppliers (Leyan reagent, Aladdin) and were used without further purification. All the reactions were carried out using a round bottom flask under a nitrogen atmosphere in anhydrous solvents. ^{1}H and ^{13}C NMR spectra were obtained in $CDCl_3$ on a WJGS-037 Bruker AVANCE III 400 MHz NMR spectrometer, using tetramethyl silane (TMS) as the internal standard. Mass spectrometry data were recorded on an Agilent 1290 Infinity. UV–vis absorbance and photoluminescence (PL) spectra were recorded on a Shimadzu UV-3600 and a Fluorescence spectrophotometer F-380 A, respectively.

2.2. Synthesis

4,5,9,10-Tetrabromo-2,7-di-*tert*-butylpyrene **1** was readily prepared by the exhaustive *tert*-butylation and bromination of pyrene by following the previously reported procedure [32]. Target compounds **TFPy** and **TTPy** were further synthesized following Scheme S1.

2.3. Synthesis of 2,7-di-tert-butyl-4,5,9,10-tetrakis-(9,9-di-methyl-fluorene) pyrene (TFPy)

To a mixture of 4,5,9,10-tetrabromo-2,7-di-*tert*-butylpyrene (300 mg, 0.48 mmol), 9,9-di-methyl-2-fluoreneboronic acid (910 mg, 3.81 mmol) and toluene (80 mL), was added CH_3CH_2OH (40 mL) at room temperature with stirring under argon. Then, a Na_2CO_3 (20%, 20 mL) solution and $Pd(PPh_3)_4$ (110 mg, 0.096 mmol) were added. The mixture was heated to 77 ºC and stirred for 24 h. After cooling, the mixture was extracted with $CHCl_3$ (100 mL × 2), washed with water and brine, dried (Na_2SO_4) and evaporated. The residue was completely dissolved in dichloromethane and purified by column chromatography with hexane: toluene (9: 1) as eluent to give **TFPy** as a white solid (65 mg, 24%). M.P. 272–274 °C; ^{1}H NMR (400 MHz, $CDCl_3$): (δ= ppm): δ_H =8.10 (d, 4H, pyrene-*H*), 7.66 (dd, *J* = 8.6, 8.0 Hz, 8H, Ph-*H*), 7.42-7. 28 (m, 20H, Ph-*H*), 1.47 (s, 18H, *t*Bu), 1.23 (d, *J* = 3.6 Hz, 24H, Me-*H*); ^{13}C NMR (100 MHz, $CDCl_3$): δ_C = 153.7, 153.0, 148.2, 139.2, 138.0, 137.2, 130.8, 130.3, 130.2, 127.2, 126.9, 126.3, 125.9, 122.5, 122.1, 121.4, 120.2, 120.0, 119.9, 119.8, 119.3, 119.0, 46.6, 35.3, 31.6, 27.1. FAB-MS: m/z calcd for $C_{84}H_{74}$ 1082.5791 [M^+]; found 1082.5838[M^+].

2.4. Synthesis of 2,7-di-tert-butyl-4,5,9,10-tetrakis-(N,N-di-phenylamino) phenyl pyrene (TTPy)

To a mixture of 4,5,9,10-tetrabromo-2,7-di-*tert*-butylpyrene (150 mg, 0.24 mmol), 4-di-phenylaminophenylboronic acid (550 mg, 3.81mmol) and toluene (40 mL), was added C_2H_5OH (20 mL) at room temperature with stirring under Argon. Then, a Na_2CO_3 (20%, 40 mL) solution and $Pd(PPh_3)_4$ (55 mg, 0.048 mmol) were added. The

mixture was heated to 77 °C and stirring for 24 h. After cooling, the mixture was extracted with $CHCl_3$ (100 mL × 2), washed with water and brine, dried (Na_2SO_4) and evaporated. The residue was subjected to column chromatography over silica gel with hexane/benzene (1:3) as eluent to give **TTPy** as a white solid (120 mg, 39%). M.P. > 300°C; ^{1}H NMR (400 MHz, $CDCl_3$): (δ= ppm): δ_H =8.07 (d, 4H, *J* = 1.6 Hz, pyrene-*H*), 7.28 (m, *J* = 8.4, 1.2 Hz, 12H, Ph-*H*), 7.26 (s, 2H, Ph-*H*), 7.25 (s, 2H, Ph-*H*), 7.20 (m, *J* = 7.6, 1.6 Hz, 8H, Ph-*H*), 7.16-7.10 (m, 24H, Ph-*H*), 7.01 (m, *J* = 10.5, 8H, Ph-*H*), 1.37 (s, 18H, *t*Bu); ^{13}C NMR (100 MHz, $CDCl_3$): δ_C = 148.1, 147.9, 146.1, 139.4, 137.7, 137.6, 135.7, 134.8, 132.3, 130.8, 129.2, 124.0, 123.9, 123.7, 122.5, 122.0, 121.9, 121.8, 35.4, 31.6. FAB-MS: m/z calcd for $C_{96}H_{78}N_4$ 1287.6260 [M^+]; found 1287.6224[M^+].

3. Results and discussion

3.1. Synthesis and characterization

In view of the electron deficiency feature of nitroaromatics and the donor-acceptor electron-transfer mechanism for sensors, electron-donating groups were introduced at the electron rich pyrene core, and two luminogens were synthesized from 4,5,9,10-tetrabromo-2,7-di-*tert*-butylpyrene **1** [32] as starting compound *via* a Suzuki coupling reaction in reasonable yields. Both compounds were fully characterized by high resolution mass spectrometry and ^{1}H and ^{13}C NMR spectroscopy (Fig. S1–4, ESI‡).

3.2. Photophysical properties

The photophysical properties of **TFPy** and **TTPy** were studied in a variety of solvents with different polarity and in the solid state; detailed parameters are presented in Table 1. Similar absorption bands with two peaks for these two compounds were observed. As shown in Fig. 1A, for the luminogen **TFPy**, there were two absorption bands centered at 260 nm and 316 nm in dilute DCM solution, while the absorption bands for

the luminogen **TTPy** were centered at 257 nm and 305 nm, respectively. The high energy absorption is mainly ascribed to the π-π* transition of the fluorenyl groups and the pyrene core. On the other hand, the low energy absorption likely results from the dominance of the locally excited (LE) state for this molecular system. Deeper explorations of the solvatochromic effects were carried out to verify this conjecture. Specifically, the absorption spectra were obtained in different organic solvents (dimethylformamide (DMF), dichloromethane (DCM), tetrahydrofuran (THF), 1,4-dioxane, and cyclohexane) of various polarities (Fig. S5, ESI‡). The maximum absorption wavelength for luminogens **TFPy** and **TTPy** exhibits a slight red-shift of ≤ 2 nm (from 315 nm to 316 nm for **TFPy**, and from 303 nm to 305 nm for **TTPy**) with the rise of the polarity of the solvent from cyclohexane to DMF. By comparison, two absorption bands of **TFPy** displayed an obvious red-shift compared with **TTPy**. Taking the absorption behavior in DCM as an example, a red-shift from 257 nm for **TTPy** to 260 nm for **TFPy** in the high energy absorption bands were observed, and a more significant change was obtained from 305 nm for **TTPy** to 316 nm for **TFPy** in the low energy absorption bands. This can be attributed to the degree of extension of the π-conjugated structure upon attachment of the peripheral substituents. The dimethyl fluorene unit plays a greater role in extending conjugation than the triphenylamine unit.

Table 1. The photophysical properties of **TFPy** and **TTPy**.

Compounds	λ_{abs}(nm) sol[a]	λ_{em}(nm) sol[b]/solid	Φ_{FL}[c] (%) sol[b]/solid	HOMO[d] (eV)	LUMO[d] (eV)	ΔE_g[d] (eV)
TFPy	260, 316	390 / 427	32 / 9.5	−5.00	−1.39	3.61
TTPy	257, 305	466 / 437	42 / 17.7	−4.81	−1.36	3.45

[a] 1×10^{-5} M in CH_2Cl_2, λ_{abs} is the absorption band appearing at the longest wavelength.

[b] 1×10^{-7} M in CH_2Cl_2, λ_{em} is the fluorescence band appearing at the shortest wavelength.

[c] Absolute quantum yield (±0.01−0.03).

[d] DFT/B3LYP/6-31G* using Gaussian.

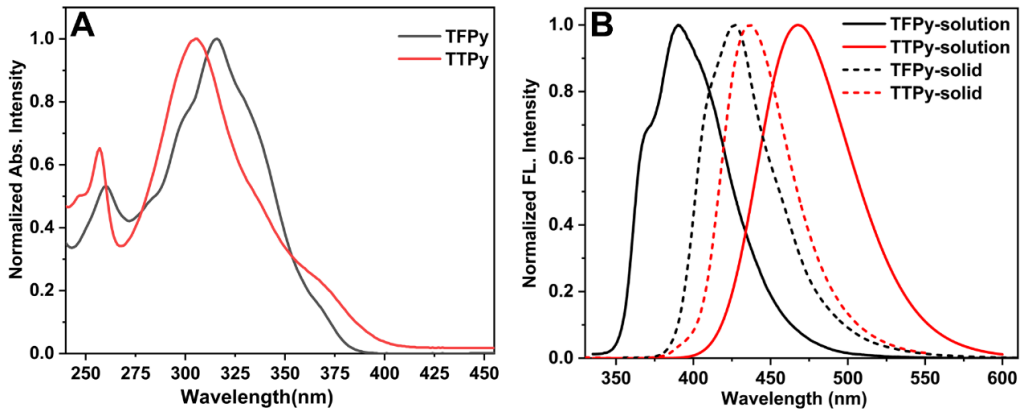

Figure 1. UV-Vis absorption (A) and emission spectra (B) for the luminogens **TFPy** and **TTPy** in DCM solution and in the solid state, respectively.

Subsequently, the emission behavior of both luminogens were recorded in diluted solvents of different polarities and in the solid state. As shown in Fig. 1B, two compounds exhibited distinct emission properties in dilute DCM solution. Due to the difference in the donating-electrons ability for the appended substituents at the K-region, the emission band of luminogen **TTPy** presents a significant red-shift of 76 nm compared to luminogen **TFPy** in DCM solution. For the former, this can be attributed to the contribution of the excimer emission due to the more remarkable ICT behavior, while the maximum emission wavelength centered at 390 nm with a deep blue fluorescence of **TFPy** results from the monomer emission [33–35].

The detailed solvatochromic effects of both luminogens in five different organic solvents with various polarities were recorded, and provides convincing evidence for the interpretation of the luminescence mechanism. As shown in Fig. 2A and Fig. S6 (ESI‡), a remarkable solvatochromic effect was observed for the emission behavior *versus* the absorption spectra. In particular for **TTPy**, a significant red-shift (from 417 nm in cyclohexane to 466 nm in DCM) was observed, which was due to the increased polarity. However, there is a seemingly irrational result, namely that the emission maximum wavelength is centered at 426 nm, which is inconsistent with the high polarity characteristics of DMF. On closer observation, a somewhat insignificant emission band at around 500 nm proves the rationality of the solvatochromic effect in DMF, and more intuitive color coordinates reveal this bathochromic shift trend using the CIE 1931 chromaticity diagram (Fig. 2B). On the other hand, the luminogen **TFPy**

displayed a slight red-shift in a series of solvents with increasing polarity (384 nm in cyclohexane, 388 nm in 1, 4-dioxane, 387 nm in THF, 390 nm DCM and 392 nm DMF) (Fig. S6 ESI‡). All the luminescence color coordinates of the luminogen **TFPy** in different diluted organic solution with deep-blue emission are concentrated in a small area (CIE: x < 0.17, y < 0.04).

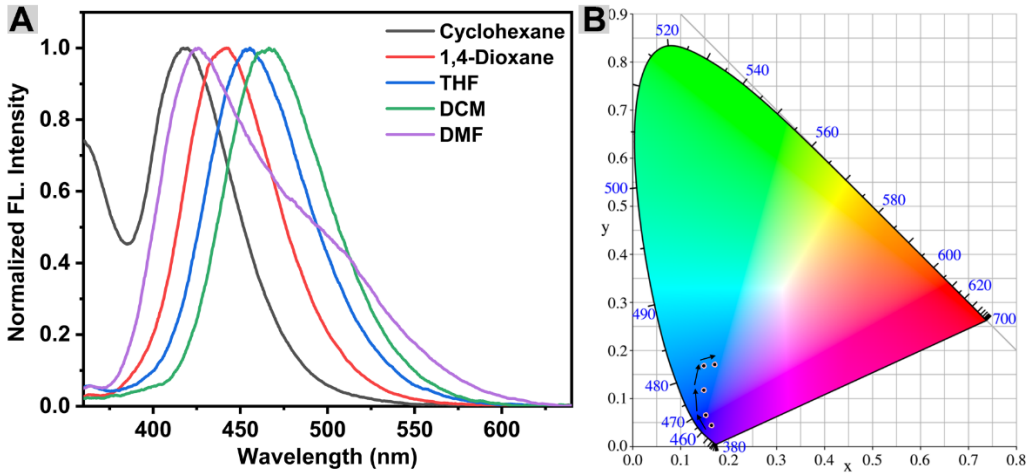

Figure 2. Solvatochromism effect in the emission spectra (A) and the CIE 1931 chromaticity diagram (B) for **TTPy** in cyclohexane, 1,4-dioxane, THF, DCM and DMF, respectively.

To further evaluate the material properties, the absolute fluorescence quantum yields (Φ_{FL}) and the emission behavior in the solid state were investigated. As compared with the emission properties in diluted solution, the emission spectra of both luminogens exhibit a small range of shift (427 nm for **TFPy**, 437 nm for **TTPy**), which may be ascribed to the dual influence of monomer emission and ICT emission [36,37]. Compared to **TFPy**, **TTPy** exhibits a red-shift of 10 nm, which can be attributed to the greater intramolecular charge transfer based on the peripheral triphenylamine units. Meanwhile, the quantum yields both in solution and in the solid state also provide more information to evaluate the current materials. As expected, both luminogens exhibit higher values for Φ_{FL} in solution (32% for **TFPy**, 42% for **TTPy**) than in the solid state (9.5% for **TFPy**, 17.7% for **TTPy**). The differences arising from the states and structures may be attributed to the distinct intramolecular charge transfer and intermolecular interactions present. In particular, a extended π-conjugated structure results from the peripheral substituents, which is more likely to form π–π interactions in the **TFPy** system, which likely results in the relatively low quantum yield. Overall,

the reasonable luminescence efficiency makes these systems promising candidates as deep-blue emitters.

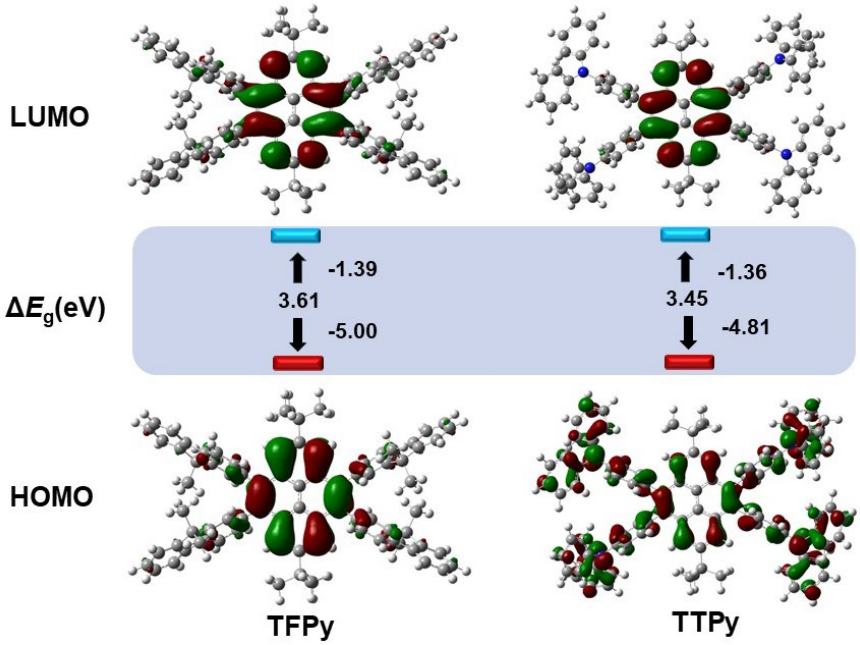

Figure 3. Frontier-molecular-orbital distributions and energy level diagrams for **TFPy** and **TTPy** by DFT calculations.

In order to verify the emission mechanism, theoretical explorations were carried out at the B3LYP/6-31g-(d) level [38,39]. As expected, the peripheral substituents at the K-region basically determined the distributions of their highest occupied molecular orbital (HOMO) and lowest unoccupied molecular orbital (LUMO). As shown in Fig. 3, the electron-donating capacity also play a vital role in tuning the HOMO–LUMO energy gap. In general, the electron-donating moieties can provide a prominent contribution to the HOMOs due to their electron-rich feature [40]. Thus, a clearly separated HOMO and LUMO distribution for the luminogen **TTPy** was observed, while the distributions of HOMO and LUMO for the luminogen **TFPy** is similar, and these are mainly located over the pyrene core. The energy gaps (ΔE_g) also gradually reduce from 3.61 eV for **TFPy** to 3.45 eV for **TTPy**. These results are consistent with the experimental observations.

Both materials were further investigated for their morphology using scanning electron microscopy (SEM). As shown in Fig. 4, the microstructures of **TFPy** (A and B) and **TTPy** (C and D) showed similar rod-like distribution with lengths of up to a

hundred micrometers. However, for luminogen **TFPy**, a more compact and slender appearance were observed, while the SEM results for luminogen **TFPy** displayed a loose-looking arrangement. This results also reveal the influence of the intramolecular interactions on the photophysical properties mentioned above [41].

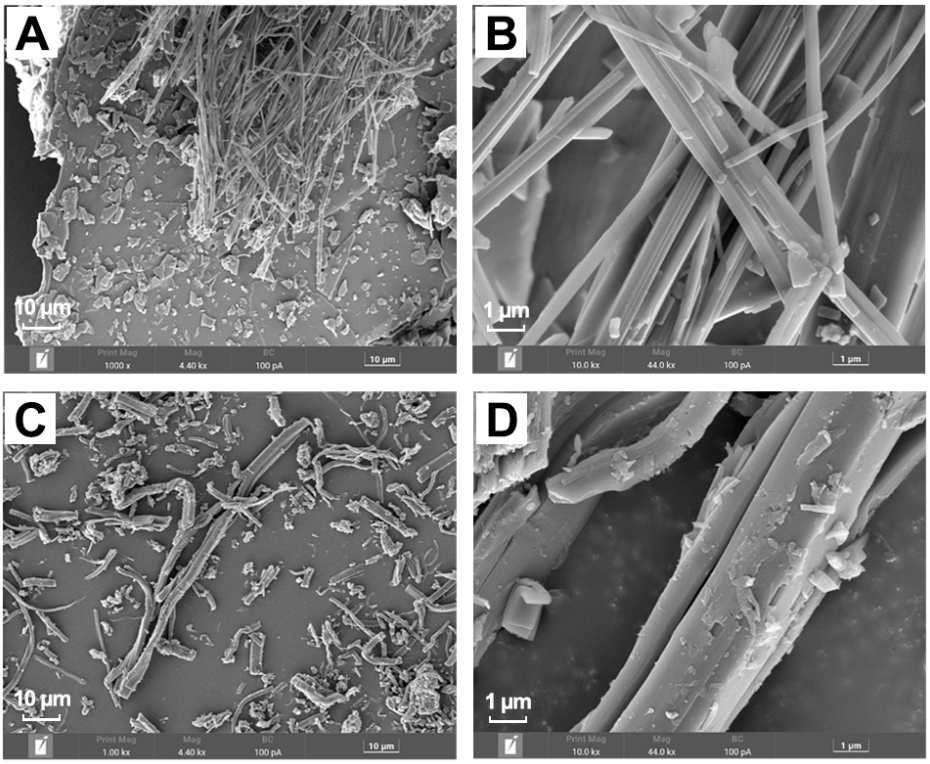

Figure 4. SEM microphotographs of powdered **TFPy** (A and B) and **TTPy** (C and D) at different magnification, respectively.

3.3. Selective detection of nitroaniline

The excellent photophysical properties of both luminogens prompted us to explore their potential applications. In view of the multiple electron-donating substituents at the periphery of the pyrene core and the extended π-conjugated structure, these potential sensor candidates were studied for the detection of electron-deficient nitroaromatics (NACs) [42].

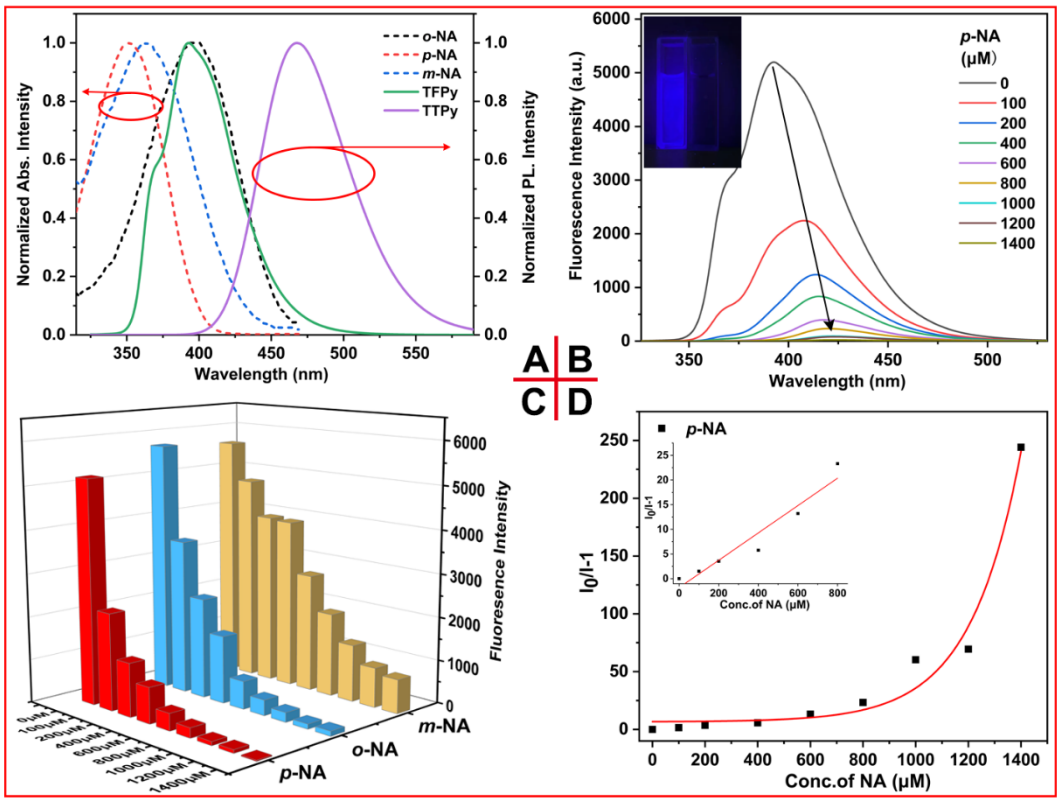

Figure 5. (A): Normalized absorption spectra of **NA** and fluorescence spectra of two luminogens in DCM; (B): Fluorescence quenching of **TFPy** on incremental addition of ***p*-NA** and inset photographs show the visible change in the fluorescence under UV light before and after addition of ***p*-NA**; (C): Histogram of the fluorescence quenching of **TFPy** with **NA**; (D): Corresponding Sterne-Volmer plots for quenching of **TFPy** with ***p*-NA** as quencher in DCM. Inset shows the Sterne-Volmer plots at lower concentration of ***p*-NA**.

Based on this prediction, a series of systematic studies were carried out to evaluate their effectiveness for the detection of nitroanilines by employing these two luminogens. As previously reported, some pyrene-based fluorescence sensors exhibit highly selective and sensitive sensing behavior based on the FRET mechanism. Thus, the absorption spectra of **NA** and the emission spectra of the luminogens are represented in Fig. 5A. Subsequently, a study was carried out to verify whether these systems are indeed capable of the sensitive recognition of **NA**. However, another result that defies the FRET mechanism was obtained. Both materials present excellent selectivity and sensitivity for ***o*-NA** (see Fig. 5 and Fig. S7–11 ESI‡). Taking **TFPy** and NA as an example, as shown in Fig. 5B, the quenching experiments were performed by adding standard DCM solutions containing different ***p*-**NA concentrations which varied from 0.1 to 1.4 mmol·L^{-1}. A sharp fluorescence quenching was observed as the concentration

of ***o*-NA** increased. The fluorescence quenching efficiency is up to 99.6%, which can be described as ultra-high detection efficiency compared to other reported pyrene-based sensors [43,44]. Moreover, for ***o*-NP** and ***m*-NA**, relatively weak quenching results (97.9% for ***o*-NP** and 86.1% for ***m*-NA**) for **TFPy** were recorded. Meanwhile, **TTPy** displayed similar quenching behavior with differentiated fluorescence quenching effciency, and the values of **TTPy** were found to be 96.3% for ***o*-NP**, 69.1% for ***o*-NP** and 76.1% for ***m*-NA**, respectively. Thus, both materials, especially **TFPy**, displayed excellent selectivity and sensitivity for **NA** as an optical sensor. The histograms show the quenching behavior more intuitively (see Fig. 5C and Fig. S12 ESI‡). This conclusion was further confirmed by the Stern–Volmer (SV) equation. As shown in Fig. 5D, a hyperbolic curved Stern–Volmer plot was found upon plotting the concentration of ***p*-NA** added *versus* the fluorescence intensity, which was also found to be linear at lower concentrations (up to 0.8 mM, inset Fig. 5D). This may be attributed to the synergistic effect of static and dynamic (collision) quenching [45]. A Stern–Volmer constant (K_{sv}) of 2.77×10^4 M^{-1} and a detection limit of 2.75×10^{-8} M were calculated for the **TFPy**/***o*-NA** system using the equation: $LOD = 3\sigma/K$. The detailed calculation procedure and results for other systems are shown in supporting information and Fig. S13 ESI‡. The experimental results revealed that the efficient and sensitive quenching response was attributed to the PET process [46].

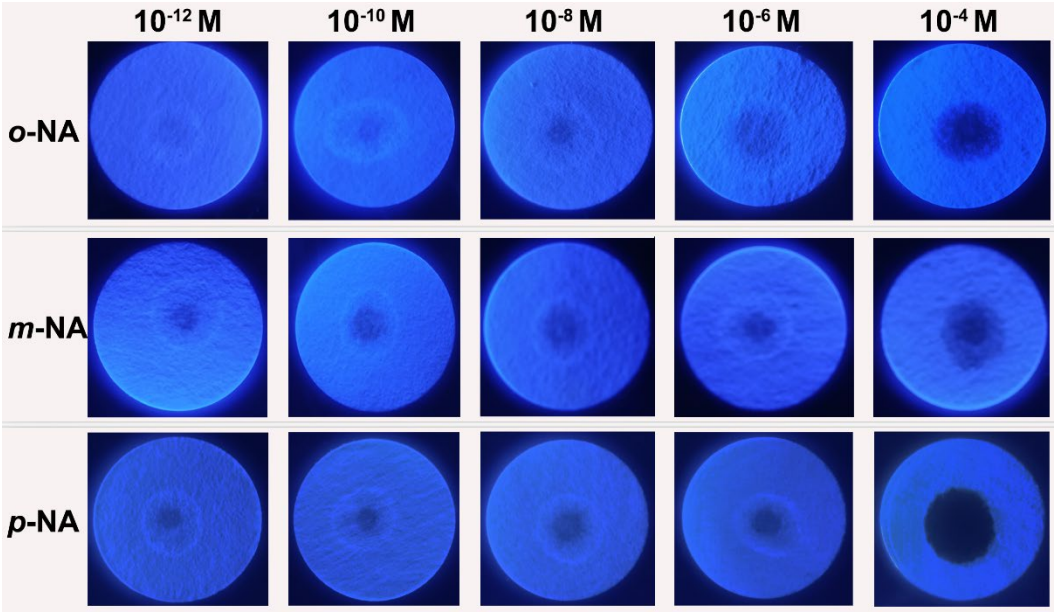

Figure 6. Test strips of **TFPy** and its response to **NA** at different concentrations under UV irradiation.

We prepared test strips by dip coating a DCM solution of **TFPy** onto qualitative filter paper followed by drying under vacuum. In order to evaluate the detection performance of trace nitro explosives, a series of solutions of **NA** at different concentration from 10^{-12} M to 10^{-4} M were prepared. As shown in Fig. 6, 8 μL of each solution was dripped onto the test strips under 365 nm UV irradiation, respectively. A visual detection result consistent with previous emission spectra results was observed, and a portable and efficient visual fluorimeter is expected to be developed to detect nitroaniline, particularly for *para*-nitroaniline.

Conclusions

In summary, two K-region tetra-substituted pyrene-based luminogens with reasonable quantum yields and deep-blue emitting were prepared, which were selected as sensors for the detection of trace nitroaniline (**NA**), including ***o*-NP**, ***m*-NA** and ***p*-NA**. Luminogens **TFPy** and **TTPy** exhibited excellent selectivity and sensitivity for ***p*-NA** with a competitive LOD as low as 10^{-8} M. More importantly, the experimental results for the visual detection exhibited increased sensitivity by the naked eye with the aid of visual test strips, and a clear quenching phenomenon was observed even by just employing an 8 μL dilute solution of concentration of 10^{-12} M. Overall, the present work provides an efficient strategy for the visual detection of trace nitro-explosives by constructing pyrene-based luminogens.

Conflicts of interest

The authors declare that they have no known competing financial interests or personal relationships that could have appeared to influence the work reported in this paper

Acknowledgements

This work was performed under the Cooperative Research Program of "Network Joint Research Center for Materials and Devices (Institute for Materials Chemistry and Engineering, Kyushu University)". We would like to thank the Natural Science Foundation of Shandong Province (Grant No. ZR2019BB067), this research used

resources of the Advanced Light Source, which is a DOE Office of Science User Facility under contract no. DE-AC02-05CH11231. CR thanks the University of Hull for support.

References

[1] R. P. Schwarzenbach, T. Egli, T.B. Hofstetter, U. von Gunten, B. Wehrli, Global Water Pollution and Human Health, Annu. Rev. Environ. Resour. 35 (2010) 109–136.

[2] X. C. Sun, Y. Wang, Y. Lei, Fluorescence based explosive detection: from mechanisms to sensory materials, Chem. Soc. Rev. 44 (2015) 8019–8061.

[3] L. Jiang, J. Wu, K. Chen, Y. Zheng, G. Deng, X. Zhang, Z. Li, K. S. Chiang, Polymer waveguide Mach-Zehnder interferometer coated with dipolar polycarbonate for on-chip nitroaromatics detection, Sensor Actuator B Chem. 305 (2020) 127406.

[4] T. K. Naqvi, A. K. Srivastava, M. M. Kulkarni, A. M. Siddiqui, P. K. Dwivedi, Silver anoparticles Decorated Reduced Graphene Oxide (rGO) SERS Sensor for Multiple Analytes, Appl. Surf. Sci. 478 (2019) 887−895.

[5] Y. Gao, F. Chu, W. Chen, X. Wang, Y. Pan, Arc-Induced Nitrate Reagent Ion for Analysis of Trace Explosives on Surfaces Using Atmospheric Pressure Arc Desorption/Ionization Mass Spectrometry, Anal. Chem. 94 (2022) 5463–5468.

[6] L. Duffin, X. Wang, J. Stoesz, Detection of volatile organic compounds in froth multiphase systems from oil sands operations using a headspace GC–MS method, Energy Fuels, 31 (2017), 11925–11931.

[7] L. Han, J. Kaesler, C. Peng, T. Reemtsma, O.J. Lechtenfeld, Online Counter Gradient LC-FT-ICR-MS Enables Detection of Highly Polar Natural Organic Matter Fractions, Anal. Chem. 93 (2021) 1740–1748.

[8] D. S. Moore, Instrumentation for trace detection of high explosives, Rev. Sci. Instrum. 75 (2004) 2499–2512.

[9] E. V. Verbitskiy, G. L. Rusinov, O. N. Chupakhin, V. N. Charushin, Design of fluorescent sensors based on azaheterocyclic push-pull systems towards nitroaromatic explosives and related compounds: A review, Dyes Pigm. 180 (2020) 108414.

[10] W. D. Wu, N. Shi, J. Zhang, X. D. Wu, T. Wang, L. Yang, R. Yang, C. J. Ou, W. Xue, X. M. Feng, L. H. Xie, W. Huang, Electrospun fluorescent sensors for the selective detection of nitro explosive vapors and trace water, J. Mater. Chem. A. 6 (2018) 18543–18550.

[11] P. Das, G. Chakraborty, S.K. Mandal, Comprehensive Structural and Microscopic Characterization of an Azine–Triazine-Functionalized Highly Crystalline Covalent Organic Framework and Its Selective Detection of Dichloran and 4-Nitroaniline, ACS Appl. Mater. Interfaces. 12 (2020) 10224–10232.

[12] S. A. A. Razavi, A. Morsali, M. Piroozzadeh, A Dihydrotetrazine-Functionalized Metal–Organic Framework as a Highly Selective Luminescent Host–Guest Sensor for Detection of 2, 4, 6-Trinitrophenol, Inorg. Chem. 61 (2022) 7820–7834.

[13] Y. Salinas, R. Martínez-Máñez, M. D. Marcos, F. Sancenón, A. M. Costero, M. Parra, S. Gil, Optical chemosensors and reagents to detect explosives, Chem. Soc. Rev. 41 (2012) 1261–1296.

[14] M. E. Germain, M. J. Knapp, J. Optical explosives detection: from color changes to fluorescence turn-on, Chem. Soc. Rev. 38 (2009) 2543–2555

[15] L. Shang, S. Dong, Design of fluorescent assays for cyanide and hydrogen peroxide based on the inner filter effect of metal nanoparticles, Anal. Chem. 81 (2009) 1465–1470.

[16] Z. S. Qian, X. Shan, L. Chai, J. Ma, J. Chen, H. Feng, A universal fluorescence sensing strategy based on biocompatible graphene quantum dots and graphene oxide for the detection of DNA, Nanoscale. 6 (2014) 5671–5674.

[17] Q. Liu, S. Yu, Z. Zhao, X. Zhang, R. Liu. Three anthracene-based bis-imidazolium salts: synthesis, structure and recognition for 2, 4-dinitrophenylhydrazine. Dyes Pigments. 173 (2020) 107983.

[18] Y. Liu, X. Xu, Y. Wei, Y. S. Chen, M. Gao, Z. J. Zhang, C. L. Si, H. P. Li, X. Y. Ji, J. J. Liang, Tailoring silver nanowire nanocomposite interfaces to achieve superior stretchability, durability, and stability in transparent conductors, Nano Lett. 22 (2022) 3784–3792.

[19] M. Gingras, One hundred years of helicene chemistry. Part 1: non-stereoselective

syntheses of carbohelicenes, Chem. Soc. Rev. 42 (2013) 968–1006.

[20] S. T. Song, J. Su, M. Telychko, J. Li, G. W Li, Y. Li, C. L. Su, J. S. Wu and J. Lu, On-surface synthesis of graphene nanostructures with π-magnetism, Chem. Soc. Rev. 50 (2021) 3238–3262.

[21] Y. H. Lee, H. Liu, J. Y. Lee, S. H. Kim, S. K. Kim, J. L. Sessler, Y. Kim, J. S. Kim, Dipyrenylcalix［4］arene-A fluorescence-based chemosensor for trinitroaromatic explosives, Chem. Eur. J. 16 (20) (2010) 5895–5901.

[22] N. Venkatramaiah, A. D. G. Firmino, F. A. A. Paz, J. P. C. Tomé, Fast detection of nitroaromatics using phosphonate pyrene motifs as dual chemosensors, Chem. Commun. 50 (68) (2014) 9683–9686.

[23] S. Pramanik, V. Bhalla, M. Kumar, Hexaphenylbenzene-based fluorescent aggregates for ratiometric detection of cyanide ions at nanomolar level: Set-reset memorized sequential logic device, ACS Appl. Mater. Interfaces. 6 (8) (2014) 5930–5939.

[24] W. Chen, N. B. Zuckerman, J. P. Konopelski, S. W. Chen, Pyrene-functionalized ruthenium nanoparticles as effective chemosensors for nitroaromatic derivatives, Anal. Chem. 82 (2) (2010) 461–465.

[25] K. H. Lee, J. K. Park, J. H. Seo, S. W. Park, Y. S. Kim, Y. K. Kim, S. S. Yoon, Efficient deep-blue and white organic light-emitting diodes based on triphenylsilane-substituted anthracene derivatives, J. Mater. Chem. 21 (2011) 13640−13648.

[26] T. M. Figueira-Duarte, K. Müllen, Pyrene-Based Materials for Organic Electronics, Chem. Rev. 111 (2011) 7260–7314.

[27] Y. Z. Liao, V. Strong, Y. Wang, X. G. Li, X. Wang, R. B. Kaner, Oligotriphenylene nanofiber sensors for detection of nitro-based explosives, Adv. Funct. Mater. 22 (4) (2012) 726–735.

[28] X. G. Li, Y. Z. Liao, M. R. Huang, V. Strong, R. B. Kaner, Ultra-sensitive chemosensors for Fe(III) and explosives based on highly fluorescent oligofluoranthene, Chem Sci. 4 (5) (2013) 1970–1978.

[29] N. Venkatramaiah, A. D. G. Firmino, F. A. A. Paz, J. P. C. Tomé, Fast detection of

nitroaromatics using phosphonate pyrene motifs as dual chemosensors, Chem. Commun. 50 (2014) 9683–9686.

[30] S. Pramanik, V. Bhalla, M. Kumar, Mercury assisted fluorescent supramolecular assembly of hexaphenylbenzene derivative for femtogram detection of picric acid, Anal. Chim. Acta. 793 (2013) 99–106.

[31] A. Kathiravan, A. Gowri, T. Khamrang, M.D. Kumar, N. Dhenadhayalan, K.C. Lin, M. Velusamy, M. Jaccob, Pyrene-Based Chemosensor for Picric Acid–Fundamentals to Smartphone Device Design, Anal. Chem. 91 (2019) 13244−13250.

[32] T. Yamato, M. Fujimoto, A. Miyazawa, K. Matsuo, J. Chem. Soc. Perkin Trans. 1 (1997) 1201–1207.

[33] C. Z. Wang, Z. D. Yu, W. X. Zhao, K. Yang, Y. Noda, Y. Zhao, X. Feng, M. R. J. Elsegood, S. J. Teat, C. Redshaw and T. Yamato, Pyrene-fused hexaarylbenzene luminogens: Synthesis, characterization, and aggregation-induced emission enhancement, Dyes Pigm. 192 (2021) 109452

[34] C. Z. Wang, H. Ichiyanagi, K. Sakaguchi, X. Feng, M. R. J. Elsegood, C. Redshaw and T. Yamato, Pyrene-based approach to tune emission color from blue to yellow, J. Org. Chem. 82 (2017) 7176–7182.

[35] M. J. Kim, M. Ahn and K. R. Wee, Facile intra- and intermolecular charge transfer control for efficient mechanofluorochromic material, Mater. Adv. 2 (2021) 5371–5380.

[36] Z. D. Yu, X. X. Dong, J. Y. Cao, W. X. Zhao, G. H. Bi, C. Z. Wang, T. Zhang, S. Rahman, P. E. Georghiou, J. B. Lin and T. Yamato, Substituent effects on the intermolecular interactions and emission behaviors in pyrene-based mechanochromic luminogens, J. Mater. Chem. C. 10 (2022) 9310–9318.

[37] Z. D. Yu, J. Y. Cao, H. L. Li, G. Yang, Z. M. Xue, L. Jiang, J. Y. Yu, C. Z. Wang, X. Y. Liu, C. Redshaw and T. Yamato, Structure-controlled intramolecular charge transfer in asymmetric pyrene-based luminogens: Synthesis, characterization and optical properties, New J. Chem. 46 (2022) 16394–16400.

[38] S. Grimme, J. Antony, S. Ehrlich and H. Krieg, A consistent and accurate ab initio parametrization of density functional dispersion correction (DFT-D) for the 94 elements H-Pu, J. Chem. Phys. 132 (2010) 154104.

[39] J. Liu, Y. Zhang, K. Zhang, J. Fan, C. K. Wang and L. Lin, Bicolor switching mechanism of multifunctional light-emitting molecular material in solid phase, Org. Electron. 71 (2019) 212–219.

[40] C. Z. Wang, R. Y. Zhang, K. Sakaguchi, X. Feng, X. Q. Yu, M. R. J. Elsegood, S. J. Teat, C. Redshaw, T. Yamato, Two-photon-absorption properties of pyrene-based dipolar D-π-A fluorophores, ChemPhotoChem. 2 (2018) 749–756.

[41] C. Z. Wang, X. Feng, Z. Kowser, C. Wu, T. Akther, M.R.J. Elsegood, C. Redshaw, T. Yamato, Pyrene-based color-tunable dipolar molecules: synthesis, characterization and optical properties, Dyes Pigm. 153 (2018) 125–131.

[42] V. Bhalla, H. Arora, H. Singh, M. Kumar, Triphenylene derivatives: chemosensors for sensitive detection of nitroaromatic explosives, Dalton Trans.42 (2013) 969–974.

[43] S.Y. Kim, M.J. Kim, M. Ahn, K.M. Lee, K.R. Wee, Systematic energy band gap control of pyrene-based donor-acceptor-donor molecules for effcient chemosensor, Dyes Pigm. 191 (2021) 109362.

[44] Z. D. Yu, J. Y. Cao, H. L. Li, G. Yang, W. X. Zhao, C. Z. Wang, S. H. Chen, M. R. J. Elsegood, C. Redshaw and T. Yamato, Crystallization-induced emission enhancement of alkyl chain-dependent pyrene-based luminogens: Visual detection of nitro-explosives, J. Lumin. 253 (2023) 119439.

[45] J. R. Lakowicz, Principles of fluorescence spectroscopy, kluwer academic/plenum publishers, New York 2nd edn. 1999.

[46] P. Das, G. Chakraborty, S. K. Mandal, Comprehensive structural and microscopic characterization of an azine−triazine-functionalized highly crystalline covalent organic framework and its selective detection of dichloran and 4-nitroaniline, ACS Appl. Mater. Interfaces, 12 (2020) 10224−10232.